Article

Fault Location Study of Overhead Line–Cable Lines with Branches

Wensi Cao [1,*] **, Lixing Zhao** [1] **, Zhaohui Li** [1] **, Jianming Chen** [2,*] **, Mingming Xu** [3] **and Rongze Niu** [3]

[1] School of Electrical Engineering, North China University of Water Resources and Electric Power, Zhengzhou 450045, China; 201710123@stu.ncwu.edu.cn (L.Z.); z20201050624@stu.ncwu.edu.cn (Z.L.)
[2] School of Electronic Information and Intelligent Manufacturing, Sias University, 168 Renmin Road, Xinzheng 451150, China
[3] State Grid Henan Electric Power Research Institute, Zhengzhou 450002, China; xu_ming_ming@vip.sina.com (M.X.); li1090528774@163.com (R.N.)
[*] Correspondence: eegscaows@ncwu.edu.cn (W.C.); cjm@ncwu.edu.cn (J.C.)

Abstract: A new fault location method based on the three-terminal travelling wave method is proposed for the fault location problem of multi-branch overhead line–cable transmission lines. Firstly, the process of fault travelling wave propagation in overhead transmission lines and the phenomenon of refraction are analysed, and an improved phase-mode transformation is introduced to decouple the electromagnetic coupling and perform fault phase selection. Secondly, the Pearson correlation coefficient is introduced to compare the similarity of the current travelling waveforms at different measurement points in order to implement fault segmentation. To solve the problems of the complexity of the fault travelling wave propagation process and the difficulty of identifying the travelling wavehead, the Hilbert–Huang transform is used to extract the fault signal characteristics, and the travelling wave arrival moment is accurately calculated by the sampling error correction method to determine the fault location. Finally, the accuracy and stability of the method are verified via a simulation test on the MATLAB/Simulink platform. The results show that the proposed positioning method combining the three-terminal travelling wave method with HHT and sampling error correction can locate the fault location more accurately, and it has good potential for application in the engineering field. It provides a new technical means for fault location in overhead transmission lines, which is expected to become one of the most important technologies in the future power system.

Keywords: fault location; three-terminal travelling wave method; fault zone determination; Hilbert yellow transformation; sampling error correction

1. Introduction

More and more hybrid overhead lines are appearing today. Such hybrid lines can combine the advantages of overhead lines and cable lines, e.g., certain long-distance transmission lines, which can take the form of hybrid lines to reduce the overall cost of using pure cable lines. On the other hand, the hybrid line is more flexible and can be used according to the specific situation. However, hybrid lines are more difficult to manage and have a relatively high failure rate due to their complex structure. At the same time, the hybrid line has the characteristics of both cable lines and overhead lines, and troubleshooting is more difficult. The problem of reducing the fault location error of hybrid overhead lines and improving the operational reliability of hybrid lines has been the focus of scholars' attention.

After decades of research, development, and application, it is apparent that the commonly used transmission line fault methods are the impedance ranging method, the fault analysis method, the intrinsic frequency method, and the travelling wave ranging method. Among them, impedance ranging is based on Ohm's law; it calculates fault impedance from voltage and current signals to determine the fault location. It is widely used because

of its low cost and the fact that it is not limited by communication conditions [1]. However, the transmission lines in the impedance ranging method are mostly equated using the centralised parameter model, ignoring their capacitive parameters, and when the transmission lines reach a certain length, the distribution effect makes the voltage and current along the transmission lines vary more obviously in the form of hyperbolic curves, which is difficult to ignore. Therefore, the fault location study of long-distance transmission lines that ignore their capacitive effects will significantly reduce measurement accuracy, which will lead to large errors in actual engineering applications [2]. Among the fault analysis methods, there are the single-end fault analysis method and the double-end fault analysis method, but the double-end fault analysis method has a data synchronisation problem. Some authors in the literature [3] have proposed an algorithm that combines parameter detection with double-end fault ranging, which overcomes the asynchronous problem of double-end measurement data in the traditional ranging method by calculating the non-synchronous angle; this algorithm is simple, requires minimal calculation, is unaffected by transition resistance, and has a wide range of applications. Related publications in the literature have [4] used the iterative search method for fault location based on the distributed parameter model. This method does not require the data synchronisation of the measurement system at both ends and can still maintain good distance accuracy at a lower sampling frequency. However, the fault line parameters are susceptible to environmental temperature changes, skin effect, and other factors, which will directly affect the distance measurement results of the fault analysis method. Therefore, it is most reasonable to use real-time line parameters for distance calculation, but in practical engineering applications, off-line data are mostly used for calculation, which makes the positioning error increase. Among the aforementioned methods, the inherent frequency method is also widely used. When faults occur in different lines, the fault travelling waves can be decomposed into different continuous spectra due to the differences in their travelling wave propagation paths, and the inherent frequency method is used to locate faults by studying the characteristics of the fault travelling wave spectrum and using the relationship between the frequency components in the travelling wave and the fault distance [5]. In the literature [6], some authors have proposed determining the fault location using the inherent frequency of the travelling wave and simulating and verifying it for conventional transmission lines. However, this method is only applicable to cases where the line protection device is tripped after a fault occurs, and the application is small. In the literature [7], it has also been found that a travelling wave spectrum can be influenced by the equivalent impedance of the line terminals. The authors extracted the main frequency of the fault travelling wave, determined the travelling wave velocity at this frequency, and combined it with information such as the fault reflection angle for fault location. Some authors in the literature [8] have used variational modal decomposition to identify and obtain the eigenfrequency, which simulates and analyses the T-shaped transmission line, proving that the method has high-range accuracy, that it is highly adaptable, and that it is less affected by confusion. Some authors in the literature [9] also propose the use of the atomic decomposition algorithm to identify the eigenfrequency after a rough analysis of the main frequency by FIR filter. Others [10] have used the Prony algorithm with high fitting accuracy to extract the eigenfrequency; it has been verified via simulation that this method locates more efficiently than the fast Fourier transform method. However, the harmonics and noise generated during the operation of the system, as well as the folded reflection phenomenon generated during the propagation of the travelling wave, will affect the identification of the intrinsic frequency and thus the ranging accuracy. The travelling wave ranging method is used to obtain the time difference between different refracted travelling waves arriving at the measurement point by analysing the complex folded reflection phenomenon generated by the wave impedance discontinuity points encountered during the transmission of the faulty travelling wave to achieve fault location [11]. The single-ended and double-ended travelling wave methods both need to calculate the travelling wave speed by substituting it into the ranging equation, while the travelling wave speed is prone to changes in line parameters, the environment, and

other factors, which brings certain errors to the fault location. The authors of [12] proposed the use of this end, the opposite end, and the line adjacent to the end of the three points of the three-end travelling wave method; this method is not affected by wave speed and can eliminate the line arc sag caused by the distance measurement error and distance measurement results. Compared to the single-ended travelling wave method, the double-ended travelling wave method is more accurate and reliable. In [13], the three-terminal travelling wave method was applied to a T-shaped line, and the wavelet transform and mode extremes were used to identify the fault travelling wavehead, and the simulation results verified that this method is still applicable in the fault line with branches and that it has high distance measurement accuracy. In [14], the three-terminal travelling wave method was applied to build a simulation model after the Ha-Zheng ±800 kV bipolar EHV DC transmission project, and it was verified through extensive simulations that this method is not affected by the fault type, thus further indicating that the three-terminal travelling wave method is robust and highly applicable. Compared with the single-ended and double-ended travelling wave methods, the three-terminal travelling wave method can eliminate the influence of travelling wave speed and line arc sag on ranging accuracy by adding more measurement points, and it is applicable to various fault types with higher accuracy.

The Pearson correlation coefficient, which is a measure of waveform similarity, is used to determine the fault segment based on the three-terminal travelling wave method and the characteristics of large differences in the current travelling waveforms on both sides of the fault point. The Hilbert–Huang Transform (HHT) is used to extract the eigenvalues of the fault signal. The complex multi-component signal is adaptively decomposed from high to low frequencies by HHT, and the instantaneous frequencies and instantaneous amplitudes of each component are derived to obtain the time-frequency distribution of the original signal, and the initial travelling wave arrival time is further corrected by using the sampling error correction method to improve the accuracy.

2. Transmission Line Travelling Wave Transmission Characteristics and Travelling Wave Distance Measuring Method

2.1. Travelling Wave Propagation Process in Overhead Lines—Cable Hybrid Transmission Lines

Figure 1 shows a folded reflection diagram of the fault travelling wave after an earthed short circuit in the overhead line–cable hybrid line.
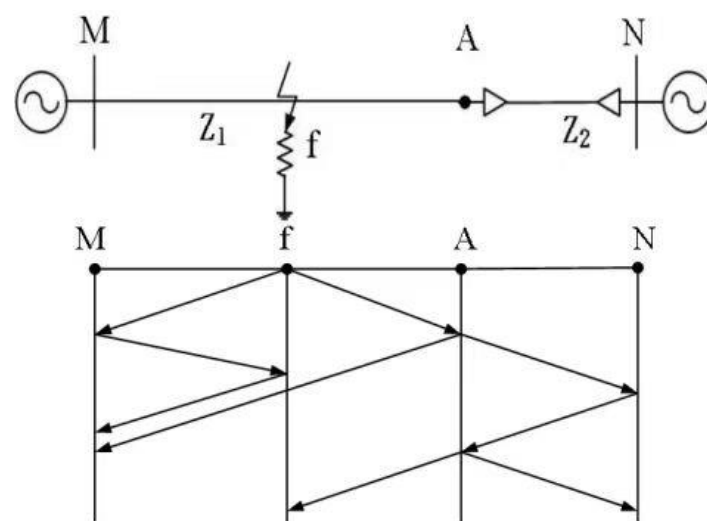

Figure 1. Fault line refraction reflection of overhead line–cable hybrid transmission line.

In a hybrid overhead contact line, a fault travelling wave will propagate through the line when a fault occurs. A fault travelling wave is a special electromagnetic wave caused by sudden changes in voltage and current, and it usually has a high frequency component.

Fault travelling waves propagate in the line along the transmission line characteristics of the conductor and also reflect and refract between the overhead line and the cable. In a complex overhead line–cable hybrid line, the propagation path and transmission characteristics of the fault travelling wave will vary depending on various factors, such as line topology, conductor diameter, distance, and cable characteristics. Typically, the fault travelling wave will propagate along the vertical distance between the adjacent wires of the line, and its speed will depend on factors such as the transmission characteristics of the line and the equivalent inductance of the cable. During transmission, the amplitude of the fault travelling wave decays, and the rate of decay depends on the resistance of the line and the resistance and conductance of the cable.

In hybrid overhead lines, the complexity of the propagation path and the transmission characteristics of the fault travelling waves make accurate fault diagnosis difficult.

2.2. Phase-Mode Transformation of Three-Phase Transmission Lines

In the actual operation of power systems, the use of three-phase transmission lines causes the electromagnetic coupling phenomenon between the phase and ground lines, which needs to be decoupled and analysed before using the travelling wave ranging method.

In a three-phase lossless commutated line, the three-phase voltages and currents, as a function of position x and time t, are given by:

$$\begin{cases} -\frac{\partial i_A}{\partial x} = (C_0 + 2C_m)\frac{\partial u_A}{\partial t} - C_m\frac{\partial u_B}{\partial t} - C_m\frac{\partial u_C}{\partial t} \\ -\frac{\partial i_B}{\partial x} = -C_m\frac{\partial u_A}{\partial t} + (C_0 + 2C_m)\frac{\partial u_B}{\partial t} - C_m\frac{\partial u_C}{\partial t} \\ -\frac{\partial i_C}{\partial x} = -C_m\frac{\partial u_A}{\partial t} - C_m\frac{\partial u_B}{\partial t} + (C_0 + 2C_m)\frac{\partial u_C}{\partial t} \end{cases} \tag{1}$$

$$\begin{cases} -\frac{\partial u_A}{\partial x} = L_s\frac{\partial i_A}{\partial t} + L_m\frac{\partial i_B}{\partial t} + L_m\frac{\partial i_C}{\partial t} \\ -\frac{\partial u_B}{\partial x} = L_m\frac{\partial i_A}{\partial t} + L_s\frac{\partial i_B}{\partial t} + L_m\frac{\partial i_C}{\partial t} \\ -\frac{\partial u_C}{\partial x} = L_m\frac{\partial u_A}{\partial t} + L_m\frac{\partial u_B}{\partial t} + L_s\frac{\partial u_C}{\partial t} \end{cases} \tag{2}$$

where C_0 is the capacitance of each phase-to-ground fault; C_m is the capacitance between phases; L_s is the self-inductance of each phase; L_m is the mutual inductance between phases. Convert (1) and (2) coefficients into matrix form; then, (3) can be obtained:

$$\begin{cases} -\frac{\partial i}{\partial x} = C\frac{\partial u}{\partial t} \\ -\frac{\partial u}{\partial x} = L\frac{\partial i}{\partial t} \end{cases} \tag{3}$$

capacitance, and inductance matrices, respectively:

$$C = \begin{bmatrix} C_0 + 2C_m & -C_m & -C_m \\ -C_m & C_0 + 2C_m & -C_m \\ -C_m & -C_m & C_0 + 2C_m \end{bmatrix} \tag{4}$$

$$L = \begin{bmatrix} L_s & L_m & L_m \\ L_m & L_s & L_m \\ L_m & L_m & L_s \end{bmatrix} \tag{5}$$

However, matrices C and L in the above equation contain non-diagonal elements, which increases the difficulty of the solution process. Therefore, the phase-mode transformation is used to convert the voltage and current phase components into the corresponding mode components with the following component transformation relations:

$$\begin{cases} u = T_u u_m \\ i = T_i i_m \end{cases} \tag{6}$$

The fluctuation equation can be obtained by taking the second derivative for the position x and time t:

$$\begin{cases} \frac{\partial^2 u_m}{\partial x^2} = T_u^{-1} LCT_u \frac{\partial^2 u_m}{\partial t^2} \\ \frac{\partial^2 i_m}{\partial x^2} = T_u^{-1} LCT_i \frac{\partial^2 i_m}{\partial t^2} \end{cases} \tag{7}$$

In Equation (7).

$$\begin{cases} T_u^{-1} LCT_u = \Lambda_u \\ T_u^{-1} LCT_i = \Lambda_i \end{cases} \tag{8}$$

Under the mode space, the non-diagonal elements of the capacitance and inductance coefficient matrices are zero, and the coefficient matrices are exchangeable matrices; therefore, there is:

$$CL = LC \tag{9}$$

Substituting into (8) gives:

$$\begin{cases} \Lambda_u = \Lambda_i = \Lambda \\ T_u = T_i \end{cases} \tag{10}$$

In Equation (10), T_u and T_i can be calculated by the eigenvalues, but their values are not unique, and the mode component consists of the zero-mode component and the line-mode component, where the line-mode component consists of the α mode and β mode components.

The conventional phase-mode transformation equation is as follows:

$$T_u = T_i = \begin{bmatrix} 1 & 1 & 1 \\ 1 & a^2 & a \\ 1 & a & a^2 \end{bmatrix} \tag{11}$$

Its inverse transformation is:

$$T_u^{-1} = T_i^{-1} = \frac{1}{3} \begin{bmatrix} 1 & 1 & 1 \\ 1 & a & a^2 \\ 1 & a^2 & a \end{bmatrix} \tag{12}$$

In the formula, $\alpha = e^{j\frac{2}{3}\pi}$.

The common phase-mode transformations are the Kellenbühl transform [15] and the Clark transform [16], but these two phase-mode transformations cannot identify the faulty phase by a single modulus, which leads to the introduction of an improved phase mode transform to solve this drawback.

Let the inverse matrix of the modified phase-mode transformation matrix S be

$$S^{-1} = \begin{bmatrix} a_{11} & a_{12} & a_{13} \\ a_{21} & a_{22} & a_{23} \\ a_{31} & a_{32} & a_{33} \end{bmatrix} \tag{13}$$

If the various fault types need to be distinguished by the α component and the β component, then there are

$$\begin{cases} a_{21} \neq a_{22} \neq a_{23} \neq 0 \\ a_{31} \neq a_{32} \neq a_{33} \neq 0 \end{cases} \tag{14}$$

set up

$$P = a_{11}a_{22}a_{33} - a_{11}a_{23}a_{32} - a_{12}a_{21}a_{33} + a_{12}a_{23}a_{31} + a_{13}a_{21}a_{32} - a_{13}a_{22}a_{31}$$

The inverse is performed to obtain the phase mode matrix S as

$$S = \begin{bmatrix} \frac{a_{22}a_{33}-a_{23}a_{32}}{p} & \frac{a_{13}a_{32}-a_{12}a_{33}}{p} & \frac{a_{12}a_{23}-a_{13}a_{22}}{p} \\ \frac{a_{23}a_{31}-a_{21}a_{33}}{p} & \frac{a_{11}a_{33}-a_{13}a_{31}}{p} & \frac{a_{13}a_{21}-a_{11}a_{23}}{p} \\ \frac{a_{21}a_{32}-a_{22}a_{31}}{p} & \frac{a_{12}a_{31}-a_{11}a_{32}}{p} & \frac{a_{11}a_{22}-a_{12}a_{21}}{p} \end{bmatrix} \tag{15}$$

The analysis shows that, for the modified phase-mode transformation to meet the requirements, it is necessary that

$$\begin{cases} a_{11} = a_{12} = a_{13} \\ a_{21} \neq a_{22} \neq a_{23} \neq 0 \\ a_{31} \neq a_{32} \neq a_{33} \neq 0 \\ a_{22}a_{33} - a_{23}a_{32} = -a_{21}a_{33} + a_{23}a_{31} = a_{21}a_{32} - a_{22}a_{31} \end{cases} \tag{16}$$

According to the conditions in Equation (4), the phase-mode transformation matrix can be constructed to increase electromagnetic coupling and the single modulus for fault phase selection, and the matrix is not unique; thus, the following phase-mode transformation matrix is used:

$$S = 24 \begin{bmatrix} 8 & 4 & 4 \\ 8 & 1 & -5 \\ 8 & -5 & 1 \end{bmatrix} \tag{17}$$

Its inverse matrix expression is given by

$$S^{-1} = \begin{bmatrix} 1 & 1 & 1 \\ 2 & 1 & -3 \\ 2 & -3 & 1 \end{bmatrix} \tag{18}$$

For different phase-mode transformation matrices, the relationship between the current component and the mode component is $i_{\alpha\beta0} = S^{-1}i_{abc}$. Where the three-phase current component and mode component are both related by the following equation:

$$\begin{cases} i_0 = i_a + i_b + i_c \\ i_\alpha = 2i_a + i_b - 3i_c \\ i_\beta = 2i_a - 3i_b + i_c \end{cases} \tag{19}$$

When a ground fault occurs in phase A, from the boundary conditions, $i_b = i_c = 0$, and this can brought into Equation (19) so that the following can be obtained:

$$\begin{cases} i_0 = i_a \\ i_\alpha = 2i_a \\ i_\beta = 2i_a \end{cases} \tag{20}$$

The above steps can be followed to derive the relationship between the zero-mode component, α mode component, and β mode component for different fault types.

The line mode components (α mode component and mode component β) obtained by using this phase-mode transformation matrix are not zero in all kinds of faults, and the fault type can only be determined by the value of α mode component or β mode component, and the zero-mode component only appears in the event of a ground short circuit, so it can easily determine whether ground short circuit occurs. The relationship between the zero-mode component, α mode component, and β mode component for different fault types is shown in the Table 1 below.

Table 1. Boundary conditions and current modulus values for various fault types. In the table, G is the ground fault.

Failure Type	Boundary Conditions	α Modal Value	β Modulus	0-Mode Component
AG	$i_{fb} = i_{fc} = 0$	$2i_{fa}$	$2i_{fa}$	i_{fa}
BG	$i_{fa} = i_{fc} = 0$	i_{fb}	$-3i_{fb}$	i_{fb}
CG	$i_{fa} = i_{fb} = 0$	$-3i_{fc}$	i_{fc}	i_{fc}
ABG	$i_{fc} = 0$	$2i_{fa} + i_{fb}$	$2i_{fa} - 3i_{fb}$	$i_{fa} + i_{fb}$
BCG	$i_{fa} = 0$	$i_{fb} - 3i_{fc}$	$-3i_{fb} + i_{fc}$	$i_{fb} + i_{fc}$
ACG	$i_{fb} = 0$	$2i_{fa} - 3i_{fc}$	$2i_{fa} + i_{fc}$	$i_{fa} + i_{fc}$
AB	$i_{fc} = 0, i_{fa} = -i_{fb}$	i_{fa}	$5i_{fa}$	0
BC	$i_{fa} = 0, i_{fb} = -i_{fc}$	$4i_{fb}$	$-4i_{fb}$	0
AC	$i_{fb} = 0, i_{fa} = -i_{fc}$	$5i_{fa}$	i_{fa}	0
ABC	$i_{fa} + i_{fb} + i_{fc} = 0$	$2i_{fa} + i_{fb} - 3i_{fc}$	$2i_{fa} - 3i_{fb} + i_{fc}$	0

Of all the short-circuit faults in the power system, single-phase earth faults are the most likely to occur; thus, single-phase earth faults are the focus of the analyses and research presented in this paper.

2.3. Three-Terminal Travelling Wave Method

The distance measuring principle of the travelling wave method mainly includes the single-ended distance measuring principle and the double-ended distance measuring principle [17], where the former calculates the fault distance by measuring the time difference between the first travelling wave arriving at the end of the line and its reflected wave [18] and the latter uses the absolute time difference between the arrival of the travelling waves at both ends of the line to calculate the distance between the fault point and the ends of the line [19,20]. The single-ended travelling wave method and the double-ended travelling wave method distance measurement principle must use the preset wave speed rather than the real-time wave speed of the line to calculate the fault distance; if the two are not the same, it will bring errors to the distance measurement results. The three-ended travelling wave method is based on the double-ended travelling wave method and adds additional measurement points by increasing the number of measurement points to eliminate the travelling wave speed, making it more difficult to measure the physical quantity. The fault travelling wave arrives at the measurement ends M, P, and N at t_M, t_P, and t_N, respectively, and PN is the fault line. A schematic diagram of the three-terminal travelling wave method is shown in Figure 2.
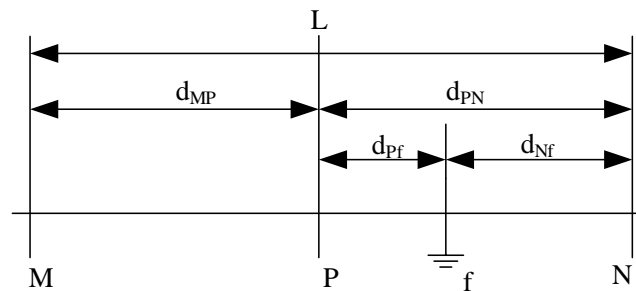

Figure 2. Principle diagram of the three-terminal travelling wave method.

Let the absolute moment of fault occurrence be t_0; assuming that the travelling wave propagation speed on the lines d_{MP} and d_{PN} is $v_{MP} \approx v_{PN} = v$, then

$$\begin{cases} (t_N - t_0)v = d_{Nf}' \\ (t_P - t_0)v = d_{Pf}' \\ (t_M - t_0)v = d_{Mf}' \\ d_{Pf}' + d_{Nf}' = d_{PN}' \end{cases} \tag{21}$$

where d_{MP}' and d_{PN}' are the paths through which the fault travels; d_{Pf}' and d_{Nf}' are the physical lengths of between the fault points and measurement point P and measurement point N, respectively.

If the line tower blocking distance and arc pitch are similar, the path through which the travelling wave propagates can be considered as the value after increasing the field line length data by a certain factor ε, that is

$$\begin{cases} (t_N - t_0)v = \varepsilon d_{Nf} \\ (t_P - t_0)v = \varepsilon d_{Pf} \\ (t_M - t_0)v = \varepsilon d_{Mf} \\ \varepsilon d_{Pf} + \varepsilon d_{Nf} = \varepsilon d_{PN} \end{cases} \tag{22}$$

where, d_{MP} and d_{PN} represent the line tower distance and the sum of the field line length, respectively; d_{Pf} and d_{Nf} represent the fault point to the measurement point P and measurement point N of the field line length, respectively. After the simplification of the above formula analysis, the following can be obtained:

(1) When the fault occurs in the MP interval,

$$d_{Nf} = \frac{(t_N - t_M)d_{MP}}{2(t_M - t_P)} + \frac{L}{2} \tag{23}$$

(2) When the fault occurs in the PN interval,

$$d_{Nf} = \frac{L}{2}\left(\frac{1}{2}\frac{2t_N - t_P - t_M}{t_M - t_P} + \frac{1}{2}\right) \tag{24}$$

Under the known conditions of d_{MP} and d_{PN}, the three-terminal travelling wave method removes the effect of wave speed, and the expression of d_{Nf} only needs to measure three time parameters. Specifically, when the fault travelling wave reaches the three points—M, P, N—for the first time, the identification of travelling wavehead first arrival time is easier and more accurate than the identification of the second time taken to reach the measurement point after reflection; compared to the single-ended travelling wave method, the double-ended travelling wave method has a higher measurement accuracy [21]. The three-terminal travelling wave method is used to calculate the fault distance because, when the two adjacent sections of the line geographical location and climate conditions are similar, the travelling waves in the two sections of the line can be regarded as the same wave speed propagation; without the introduction of travelling wave propagation speed, it is difficult to measure the physical quantity, and the method in the tower distance and line arc sag is, to a certain extent, similar to the previous case to eliminate the impact of line arc sag on the accuracy of distance measurement.

3. Mixed-Line Fault Segment Determination and Fault Signal Feature Extraction

Firstly, the entire hybrid transmission line is replaced into multiple cell segments, and the fault current travelling waves are collected at the boundary points of each segment, and the Pearson correlation coefficients of the current travelling waves of each segment are compared to determine the fault occurrence segment and improve the accuracy of fault location.

The technical difficulty of using the travelling wave ranging method for fault location lies in extracting the characteristics of the fault signal, i.e., determining the arrival time of the fault travelling wavehead, and the commonly used wavehead identification methods are Fourier transform, wavelet transform, mathematical morphology method, and Hilbert–Huang transform. The Fourier transform method is able to detect the sudden change point by extracting the mode maximum value of the travelling wavehead, and the rate of change in the travelling wave signal tends to be zero according to this feature after the transformation, but the Fourier transform method has certain limitations for non-smooth signals. Consequently, some scholars have proposed the use of the wavelet transform method to identify waveheads. The wavelet transform method has the function of time-frequency localisation, but it can only perform mechanical decomposition without adaptivity. Regarding the use of the mathematical morphology method to identify waveheads, it is more prone to its own inherent structure, and the fault travelling wave propagation path in the attenuation and other phenomena render the corresponding algorithm inapplicable. The Hilbert–Huang transform method used in this paper can adaptively decompose complex multi-component signals from high to low frequencies and obtain the instantaneous frequency and amplitude of each component to obtain the time-frequency distribution of the original signal [22].

3.1. Pearson Correlation Coefficient

The Pearson correlation coefficient is commonly used to measure the correlation between two variables *X* and *Y* [23,24]; the calculation is used to measure the similarity of the current travelling waveform on both sides of the fault point.

The ratio of the covariance and standard deviation of the two variables *X* and *Y* is the Pearson correlation coefficient between the two variables $\rho_{(X,Y)}$, as shown in the following formula:

$$\rho_{(X,Y)} = \frac{\text{cov}(X,Y)}{\sigma_x \sigma_y} = \frac{E[(X - \mu y]}{\sigma_x \sigma_y} = \frac{\sum\limits_{i=1}^{n}(X_i - \overline{X})(Y_i - \overline{Y})}{\sqrt{\sum\limits_{i=1}^{n}(X_i - \overline{X})^2 \sum\limits_{i=1}^{n}(Y_i - \overline{Y})^2}} \tag{25}$$

From Equation (11), it can be seen that when the two waveforms are more similar in *X* and *Y*, the Pearson correlation coefficient of $\rho_{(X,Y)}$ is approximately equal to 1; when the two waveforms are differ more, the Pearson correlation coefficient of $\rho_{(X,Y)}$ is not equal to one.

The Pearson correlation coefficient is determined by both the covariance and standard deviation values of the two variables. Although the covariance value alone can also measure the similarity of waveforms, the covariance is susceptible to the influence of the magnitude [25]; combining the covariance and standard deviation to judge the similarity of waveforms yields higher accuracy and correctness.

3.2. Zone Detection

When a fault occurs, the measured fault current travelling wave signals at points M, P, and N are i_1, i_2, and i_3 respectively, and three Pearson correlation coefficients can be obtained by combining these three fault current signals in two groups. When the fault occurs in the MP section of the overhead line, the measuring points P and N are located on the same side of the fault point, and their current waveforms are very similar, while the measuring points P, N, and M are located on both sides of the fault point, and their current waveforms are very different.

3.3. Hilbert–Huang Transformations Basic Theory

(1) Instantaneous frequency

In non-linear signal analysis, transient characteristics, including transient amplitude, transient frequency, and transient phase, are important [26].

Let $X(t)$ be an arbitrary time series signal which is transformed via the Hilbert–Huang method to $Y(t)$; then, the relationship is as follows:

$$Y(t) = \frac{1}{\pi} \int\limits_{-\infty}^{+\infty} \frac{X(t)}{t - \tau} d\tau \tag{26}$$

$$X(t) = \frac{1}{\pi} \int\limits_{-\infty}^{+\infty} \frac{Y(t)}{t - \tau} d\tau \tag{27}$$

In the above equations, $X(t)$ and $Y(t)$ are complex conjugate pairs, and both have time series correlation, meaning that the analytic signal is as follows:

$$\begin{cases} Z(t) = X(t) + jY(t) = A(t)e^{j\theta(t)} \\ A(t) = \sqrt{X^2(t) + Y^2(t)} \\ \theta(t) = \arctan(\frac{Y(t)}{X(t)}) \end{cases} \tag{28}$$

where $A(t)$ is the instantaneous frequency of the signal, and $\theta(t)$ is the frequency phase of the signal. Another instantaneous parameter can be obtained from $\theta(t)$:

$$f(t) = \frac{1}{2\pi} \frac{d\theta(t)}{dt} \tag{29}$$

(2) Intrinsic modal function

In practice, the signal often contains more than one oscillation mode. Through the above analysis, it can not be decomposed into the full frequency of the original signal; the signal should first be decomposed into a number of intrinsic mode functions (Intrinsic Mode Function, referred to as IMF).

The IMF has the following conditions:

①　The number of zeros in the original signal equals or differs by one from the number of extreme points, and the decomposed IMF has an extreme value greater than zero and a minimum value less than zero.

②　The upper and lower envelopes are zero, and the upper and lower envelopes are local maxima and minima, respectively. This requirement ensures the symmetry of the IMF and prevents large fluctuations in the instantaneous frequency due to the asymmetry of the signal, giving the required instantaneous frequency a practical physical meaning.

(3) Empirical modal decomposition

The most important part of HHT is Empirical Mode Decomposition (EMD), which separates multiple IMFs from a non-stationary non-linear complex signal known as the screening process because most signals cannot satisfy the IMF conditions at any time, so the signal must first be screened; then the IMFs are subjected to the Hilbert transform. This process means that the IMF components can be linear or non-linear [27].

The EMD decomposition steps are as follows:

① Calculate all polar values of the original signal $X(t)$ and fit the upper and lower envelopes.

② Calculate the average of the upper and lower envelopes e_1 and the original signal $X(t)$ minus e_1 to obtain the new sequence h_1:

$$h_1 = X(t) - e_1 \tag{30}$$

If h_1 satisfies the IMF condition, then h_1 is the first IMF component of the original signal, which is noted as $c_1 = h_1$.

③ If h_1 does not satisfy the condition, repeat steps (1) and (2) to obtain h_1 as the original signal and the up and down packets of h_1.

The complex line is recorded as e_{11}; calculate $h_{11} = h_1 - e_{11}$ and determine whether h_{11} meets the conditions of IMF. If it does, record h_{11} as c_1; if it does not, continually repeat steps (1) and (2) until h_{1k} meets the conditions and record h_{1k} as c_1.

④ Separate the first IMF component c_1 from:

$$r_1 = X(t) - c_1 \tag{31}$$

⑤ Repeat the above steps for c_1 as the original signal until a component satisfying the IMF condition is obtained as c_2. Repeat this process to obtain n IMF components of the original signal $X(t)$.

$$\begin{cases} r_1 - c_2 = r_2 \\ \dots \\ r_{n-1} - c_n = r_n \end{cases} \tag{32}$$

⑥ The loop termination condition is that the remaining quantity r_n is a monotonic function, i.e., there are no longer any extreme and extreme small values from which the IMF component can be extracted. The final decomposition takes the form of

$$X(t) = \sum_{i=1}^{n} c_i(t) + r_n \tag{33}$$

where c_i is the IMF component of the original signal $X(t)$, and r_n is the residual.

The EMD decomposition tree of the original signal $X(t)$ is shown in Figure 3:
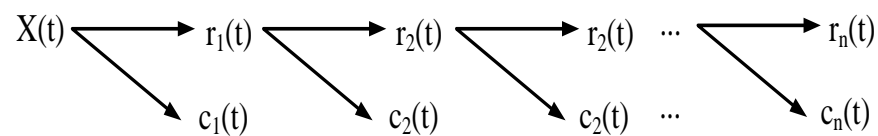

Figure 3. EMD tree.

The first IMF component of the original signal is the highest frequency component and contains important information about the fault location, so the first IMF component of the original travelling wave signal is used for fault location.

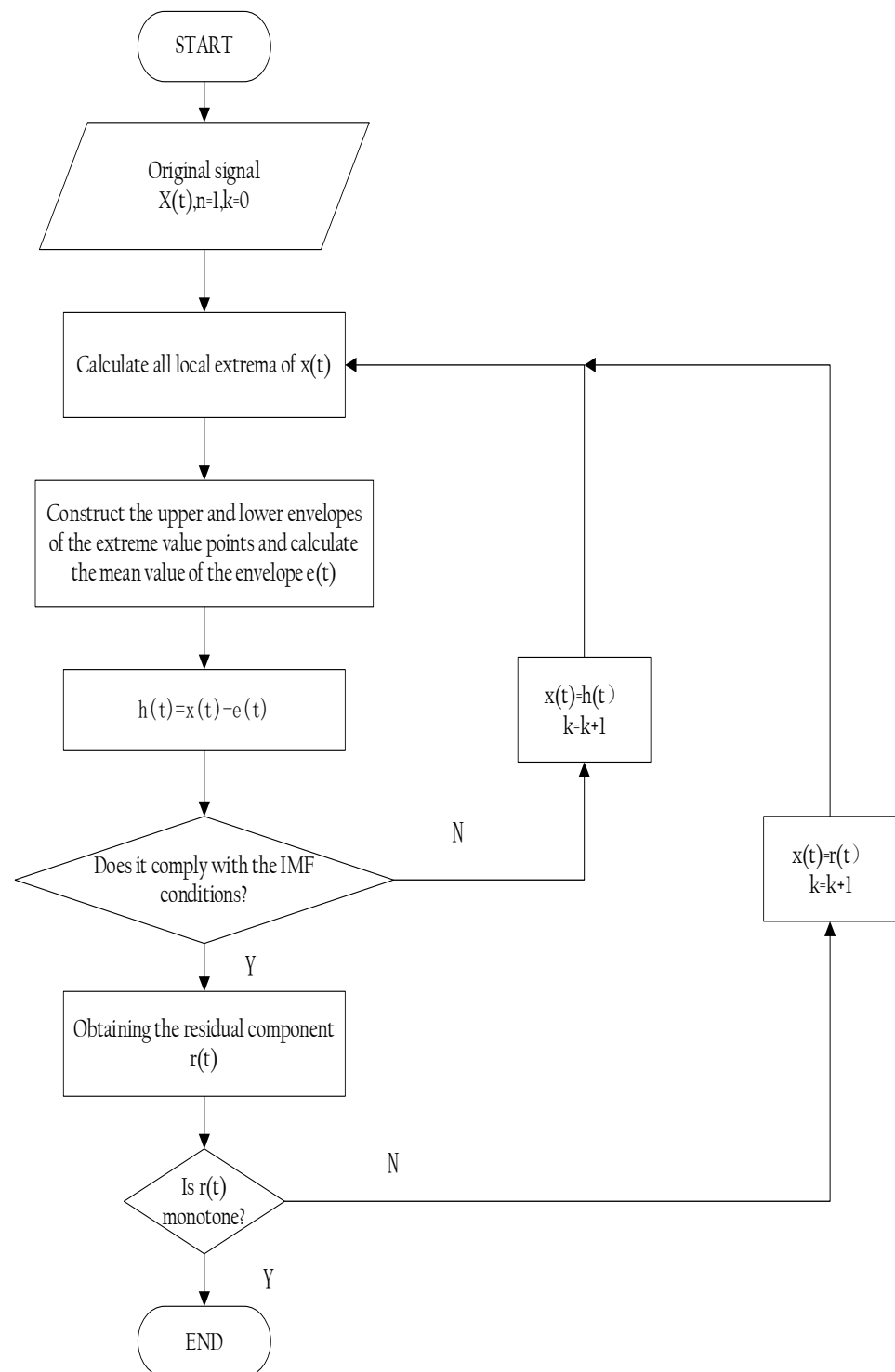The EMD decomposition flow chart is as follows (Figure 4).

Figure 4. EMD decomposition flow chart.

3.4. Hilbert's Boundary Spectrum and Energy Spectrum

As introduced in the previous section, the original signal $X(t)$ is decomposed to obtain the IMF components, and each IMF component is subjected to Hilbert Spectrum Analysis (HSA) using the following equation:

$$\hat{c}_i(t) = \frac{1}{\pi} \int_{-\infty}^{+\infty} \frac{c_i(t)}{t - \tau} \tag{34}$$

The resolution signal is

$$z_i(t) = c_i(t) + j\hat{c}_i(t) = A_i e^{j\varphi_i t} \tag{35}$$

Among them,

$$\begin{cases} A_i(t) = \sqrt{c_i^2(t) + \hat{c}_i^2(t)} \\ \varphi_i(t) = \arctan[\frac{\hat{c}_i(t)}{c_i(t)}] \end{cases} \tag{36}$$

The instantaneous frequencies of each IMF component are

$$\omega_i(t) = \frac{d\varphi_i(t)}{dt} \tag{37}$$

The original signal $s(t)$ is expressed as

$$s(t) = \text{Re}[\sum_{i=1}^{n} A_i e^{j\varphi_i t}] = \text{Re}[\sum_{i=1}^{n} A_i e^{j\int \omega_i(t)dt}] \tag{38}$$

The Hilbert spectrum of the signal is

$$H(\omega, t) = \text{Re}[\sum_{i=1}^{n} A_i e^{j\int \omega_i(t)dt}] \tag{39}$$

Integrating $H(\omega, t)$ over time, the Hilbert's boundary spectrum is obtained as follows:

$$h(\omega, t) = \int_0^T H(\omega, t)dt \tag{40}$$

Furthermore, Hilbert's energy spectrum can be obtained $E(\omega)$:

$$E(\omega) = \int_0^T H^2(\omega, t)dt \tag{41}$$

when a short-circuit fault occurs in the power system, the fault point generates a high-frequency fault travelling wave that contains rich fault information, and this signal is a sudden change signal with singularity. Therefore, the identification and analysis of the fault travelling wavehead becomes the key to fault location.

Due to the short duration of the fault transient process of the power system, the transmission process of the fault travelling wave is accompanied by folding reflection and attenuation phenomena, and the propagation characteristics and attenuation characteristics of different modes and frequency components are different, which makes the identification and detection of the travelling wavehead more difficult [28]. Therefore, the EMD decomposition of the faulty travelling wave signal is selected to extract each IMF component, the Hilbert transform of the IMF1 component is used to obtain its instantaneous spectrum, and the first high-frequency mutation point of the spectrum is used to determine the arrival time of the transient travelling wavehead to realise the fault location via the travelling wave ranging method [29].

3.5. Sampling Error Correction

An important factor affecting the accuracy of fault location is the size of the sampling frequency of the travelling waveform. The higher the sampling frequency, the higher the accuracy of the travelling waveform arrival time identification; however, the more complex the high-frequency noise components, the greater the impact on the travelling waveform identification. As the sampling frequency increases, the larger the amount of data acquired

by the travelling waveform ranging equipment, the longer the processing time, which is not conducive to the rapid acquisition of fault distance [30].

The sampling error correction method is used to further reduce the error without increasing the sampling frequency. The wavelength diagram of the local travelling waveform is shown in Figure 5, and the sampling error correction steps are as follows.
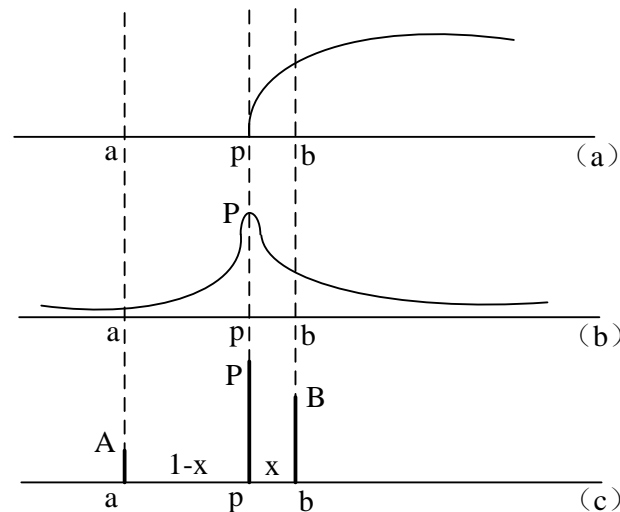

Figure 5. Local travelling wave waveform. (**a**) Faulty travelling wave local diagram. (**b**) Local waveform of the IMF1 component. (**c**) Local derivative diagram of the fault travelling wave.

(1) To determine the approximate time of arrival of the fault travelling wavehead. Let the fault current travelling waveform be as it is shown in Figure 5a. We assume that the arrival time of the true wavehead is located at point P and that a and b are the adjacent sampling points on both side of the true wavehead. After HHT decomposition, it can be roughly determined that the arrival time of the travelling wavehead is located at point a or b. Figure 5b can be obtained by locally enlarging the IMF1 component after EMD decomposition. From the above analysis, it can be seen that the true implementation of the wavehead point P is the mutation point, a localisation derivative absolute value of the largest point; with increasing closeness to point P, the derivative value becomes larger. When farther away from point P, the derivative value is smaller. After using the derivative to obtain Figure 5c, consequently, A, B should be the points a, b corresponding to the absolute value of the derivative. Set point a to the wavehead point P distance for $1 - x$. The distance from point b to point P for x, 1 is the unit sampling frequency time interval, which, according to Figure 5c, can be obtained when there is a point b before the existence of a smaller value of the derivative of the point a. This means that the true-implementation wavehead, having been calculated from the point b sampling time in advance, is located between points a and b (slightly closer to point b).

(2) The calculation of the actual wavehead—the previous step in the analysis can be derived from the moment of arrival of the true wavehead for the derivative of the absolute maximum value of the point, and in the analysis of the discrete sampling signal, it is generally used to approximate the derivative of the shape of the difference; therefore, the closer the true wavehead is to the travelling waveform, the greater the value of difference, that is, the larger the derivative; similarly, the farther away from the true wavehead, the smaller the value of the derivative. There is a linear relationship between the value of the derivative at any point and the distance from the wavehead.

$$\frac{B}{A} = \frac{1 - x}{x} \tag{42}$$

Namely:

$$x = \frac{A}{A + B} \tag{43}$$

Assuming that the measured point b is equal to the number of sampling points N, the actual position of the travelling wavehead should be equal to the number of sampling points according to the above formula $N - x$. By substituting the sampling-error-corrected arrival position of the travelling wavehead into the range equation in the previous section, the range error can be reduced.

4. Multi-Branch Overhead Line–Cable Hybrid Line Fault Location Method

Fault location flowchart of a hybrid overhead power line using the travelling wave ranging principle is in Figure 6 below.
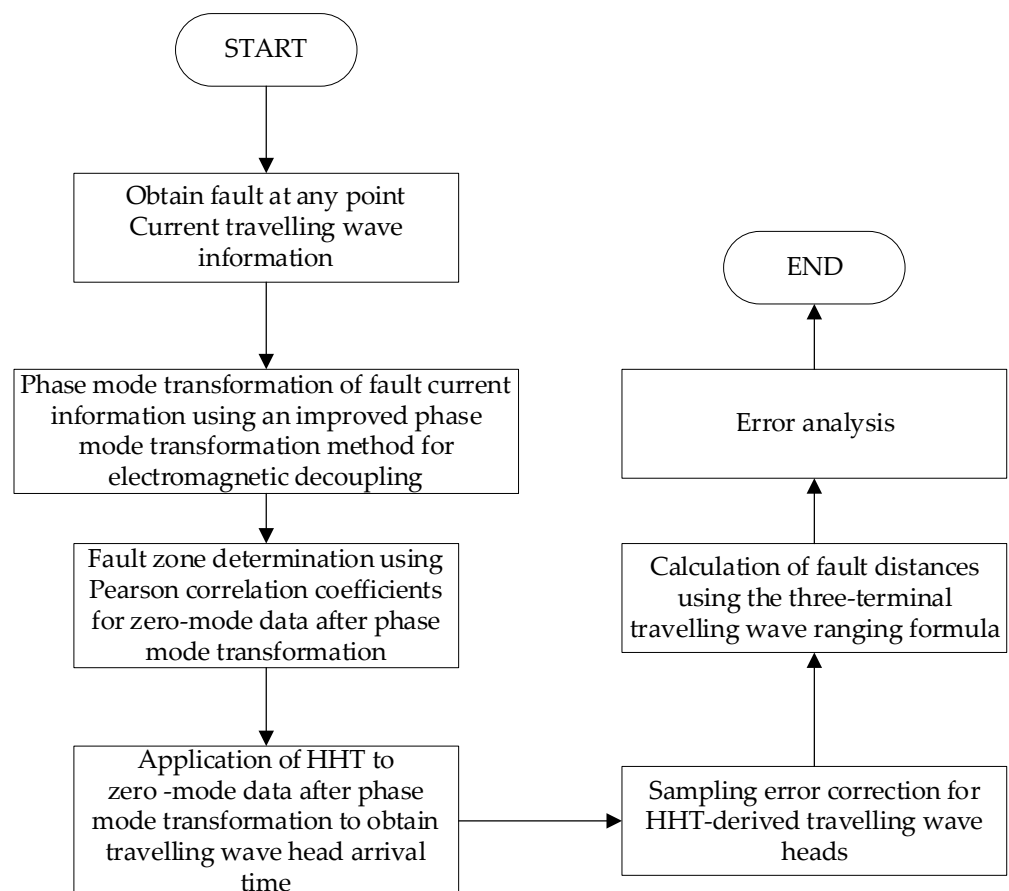

Figure 6. Fault location flowchart of a hybrid overhead power line using the travelling wave ranging principle.

Step 1: To obtain current information at each node, appropriate sensing devices, such as inductive sensors, need to be installed in the power system, and the data should be recorded and analysed by connecting to a data acquisition system. This can be achieved using a large number of high-accuracy sensors and data acquisition systems, and the data can be processed and analysed to improve the quality and accuracy of the results.

Step 2: The improved phase-locking technique can effectively decouple the original fault current signal to eliminate problems such as electromagnetic coupling, and the improved phase-mode transformation is usually used to achieve signal decoupling. The phase relationship and time-shift relationship of the signal obtained in step 1 are constrained to a phase-mode reference waveform to achieve signal decoupling and improve calculation accuracy and precision.

Step 3: The Hilbert–Huang transform is used to decompose and analyse the phase-mode transformed signal to determine the peak time of the transient travelling wave. The signal obtained after the phase-mode transformation in step 2 is first decomposed into several intrinsic mode functions (IMF) via Empirical Mode Decomposition (EMD), which is called the screening process because most of the signals cannot satisfy the IMF condition at any time. Since most signals cannot satisfy the IMF condition at any time, the signals must first be screened, and then Hilbert Spectrum Analysis (HSA) is performed for each IMF component. By analysing the spectrum and finding the first high-frequency mutation point, the peak time of the transient travelling wave can be determined to improve the accuracy and reliability of the results.

Step 4: The sampling error correction method can improve the accuracy and precision of the results; the error correction method mentioned in 2–6 above is used in the true implementation of the wavehead arrival time for the derivative of the absolute maximum value of the point, so the high-frequency mutation points obtained in step 3 will use the difference form to approximate the derivative to obtain a more accurate wavehead time.

Step 5: The results obtained are recorded and organised, and an error analysis is performed using uncertainty analysis methods to evaluate the degree of influence of various errors on the accuracy and reliability of the results to ensure the reliability and accuracy of the results. In this step, the results are calculated and compared using other algorithms and the HHT used above, and then the errors are calculated under different transition resistances to verify the correctness of the algorithm.

5. Overhead Line–Cable Hybrid Line Fault Location Simulation Analysis

5.1. Simulation Model

We used the MATLAB power system toolbox to build a multi-branch overhead line–cable hybrid line with a total length of 70 km, branch I length of 40 km, voltage level of 110 kV, and 50 Hz dual power supply system and performed sampling for a total duration of 0.05 s. After 0.016 s, a single-phase ground fault occurred, and the transition resistance was 100 Ω; the overhead line length was 50 km, and the cable line length was 20 km. The branch I overhead line length was 30 km, and branch I cable line length is 10 km, as shown in Figure 7.
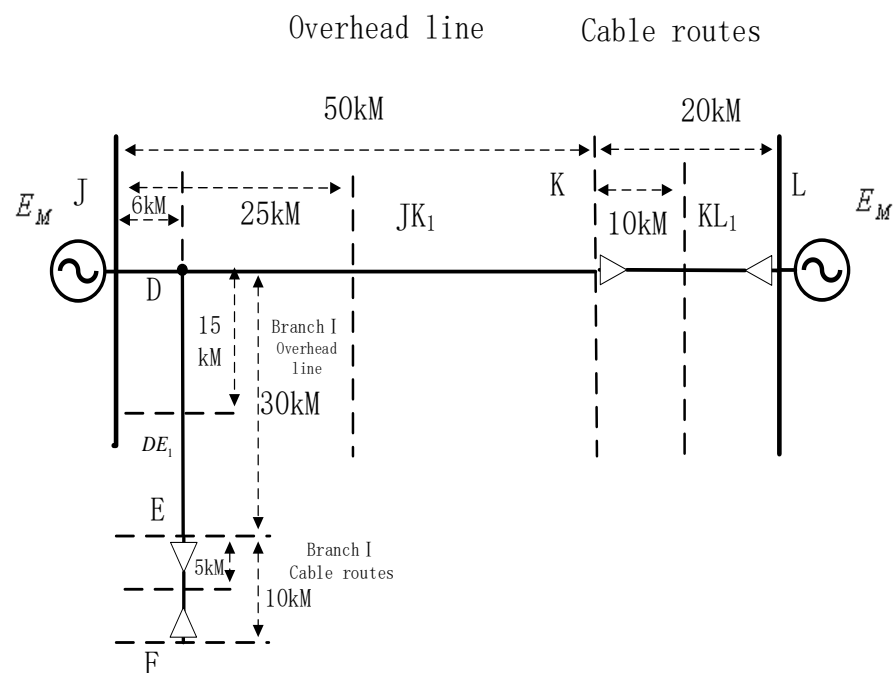

Figure 7. Schematic diagram of the overhead line–cable hybrid transmission line model.

In total, six fault points were randomly selected: overhead line section—6 km, 34 km; cable section—54 km, 63 km; branch I overhead line—6 km; branch I cable section—33 km. After carrying out the single-phase ground-short-circuit situation simulation analysis, the final fault location was determined. The distance measurement error is

$$\varepsilon\% = \frac{\text{fault location/km} - \text{fault ranging/km}}{\text{total line length/km}} \tag{44}$$

5.2. Fault Zone Determination

The Pearson correlation coefficient is used to compare the zero-mode components of the current travelling waves collected at points J, K, and L to determine the fault zone, and the sampling frequency (1 MHz) is consistent with the subsequent fault location.

Taking the example of a single-phase earth short circuit on a 6 km overhead line, the fault waveforms collected at points J, K, and L are in Figure 8 below.
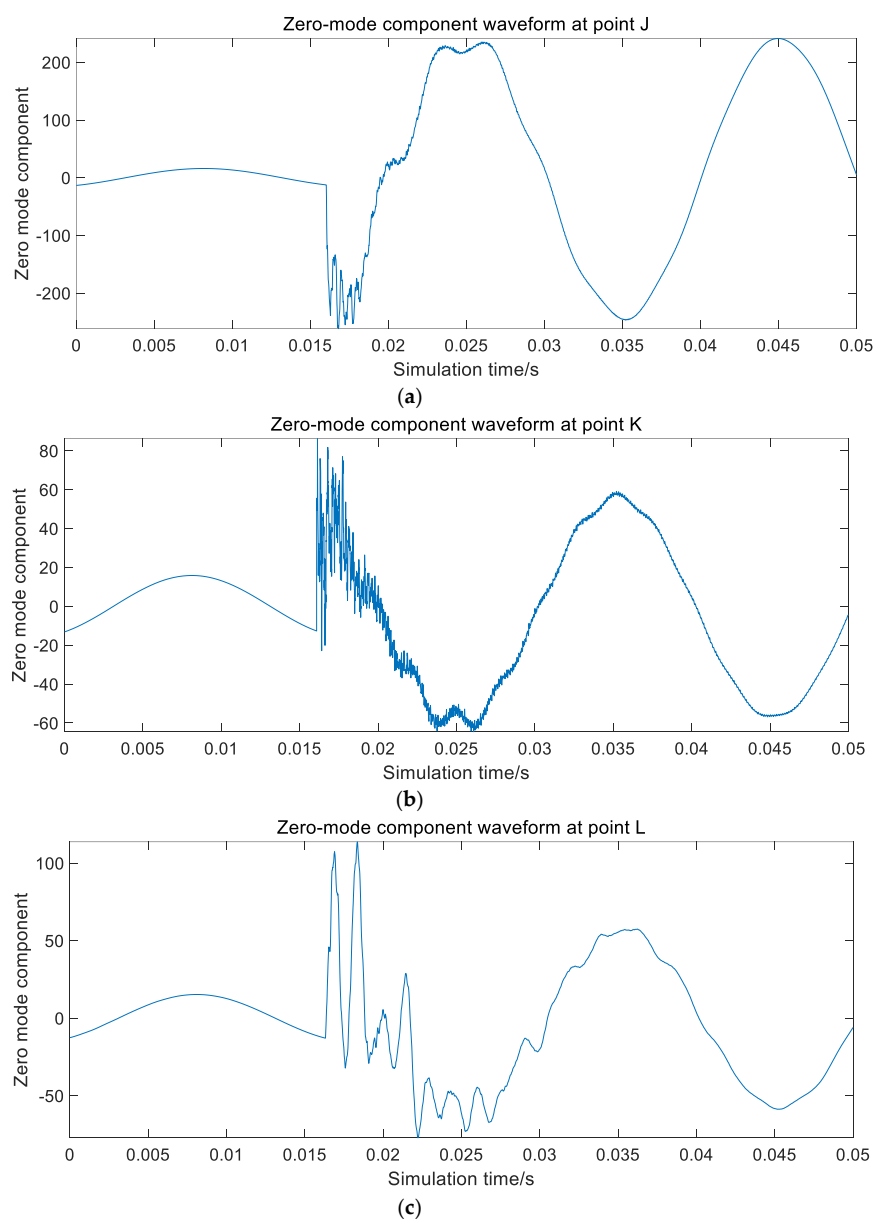

Figure 8. Zero-mode component waveforms at points J, K, and L. (**a**) Zero-mode component waveform at point J. (**b**) Zero-mode component waveform at point K. (**c**) Zero-mode component waveform at point L.

Calculate the Pearson correlation coefficients between the measurement points J and K, J and L, and K and L, respectively.

From the below Table 2, the $\rho(J,K)$ and $\rho(J,L)$ values are close to -1, indicating that the point J and point L, K waveforms differ; the $\rho(K,L)$ value is close to 1, indicating that the point K, L waveform is more similar to the judgement of the fault that occurred in the overhead line JK section.

Table 2. Pearson correlation coefficients between J and K, J and L, and K and L. (Fault on JK section of overhead line).

	$\rho(J,K)$	$\rho(J,L)$	$\rho(K,L)$
Pearson correlation coefficient	-0.9295	-0.9154	0.9076

Following the same steps as above, the remaining fault points (11 km, 34 km, 54 km, 63 km, branch I—6 km, branch I—33 km) were determined by the fault section, and the relative Pearson coefficients and the fault section determination results for different fault locations are shown in Table 3.

Table 3. Pearson correlation coefficients between J and K, J and L, and K and L.

Fault Location /km	$\rho(J,K)$	$\rho(J,L)$	$\rho(K,L)$	Fault Section
34	-0.9102	-0.9042	0.9628	Overhead line JK section
54	0.9882	-0.7493	-0.7621	Cable KL section
63	0.9819	-0.7458	-0.7573	Cable KL section

Pearson correlation coefficients between D and E, D and F, and E and F are in Table 4 below.

Table 4. Pearson correlation coefficients between D and E, D and F, and E and F.

Fault Location/km	$\rho(D,E)$	$\rho(D,F)$	$\rho(E,F)$	Fault Section
Branch I 6 km	0.1733	-0.2783	0.0261	Overhead line DE section
Branch I 33 km	0.9997	-0.2017	-0.2022	Cable EF section

The simulation analysis shows that it is feasible to use the Pearson correlation coefficient to compare the similarity of the current travelling waves on both sides of the fault point for fault zone determination.

5.3. Fault Location Based on Travelling Wave Ranging Method

The three-terminal travelling wave method avoids the identification of the folded reflection wavehead by increasing the number of measurement points, and the calculation no longer includes the travelling wave propagation speed parameter, which can eliminate the influence of line arc sag on the distance measurement accuracy to a certain extent when the tower distance and arc sag are similar.

(1) Overhead line fault location

Taking the example of a single-phase earth short circuit on a 6 km overhead line, the waveform of the zero-mode component of the measuring point JK_1 is in Figure 9 below.
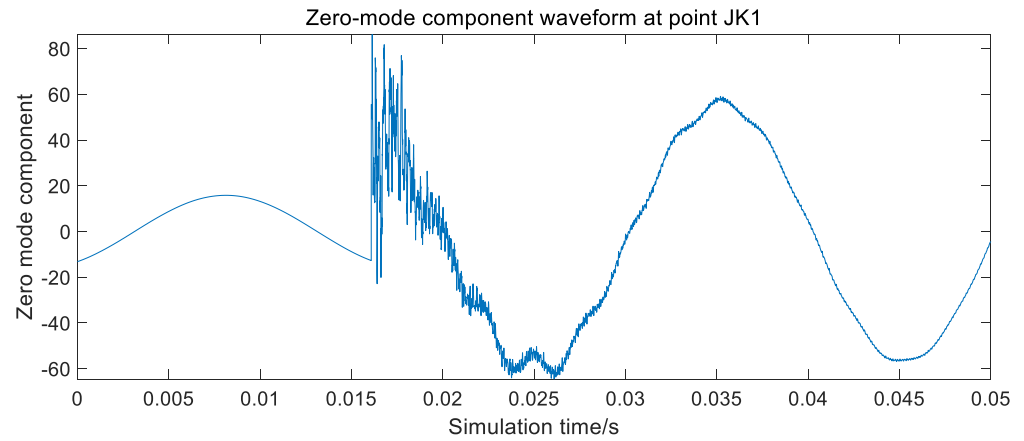

Figure 9. Zero-mode component waveform at point JK_1.

The EMD decomposition of the zero-mode component yields the following waveforms for each IMF component (Figure 10).
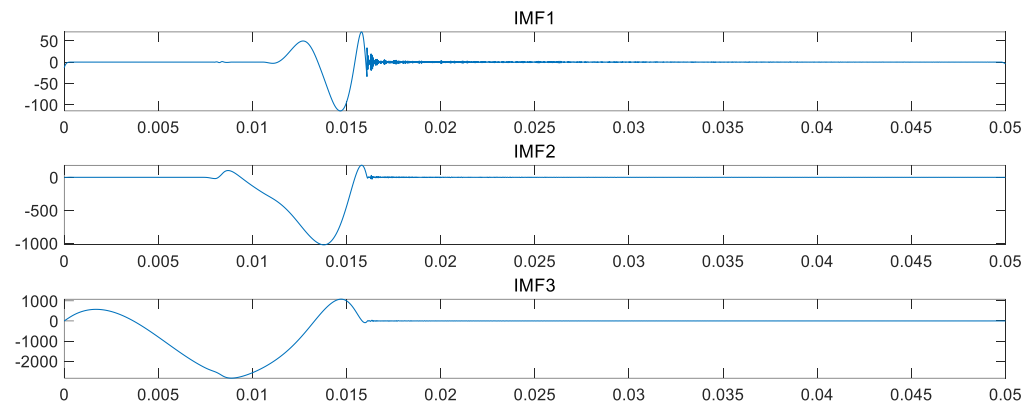

Figure 10. Point zero-mode components of each IMF component diagram.

The Hilbert transform is applied to the IMF1 component to obtain its local instantaneous spectrum as follows (Figure 11).
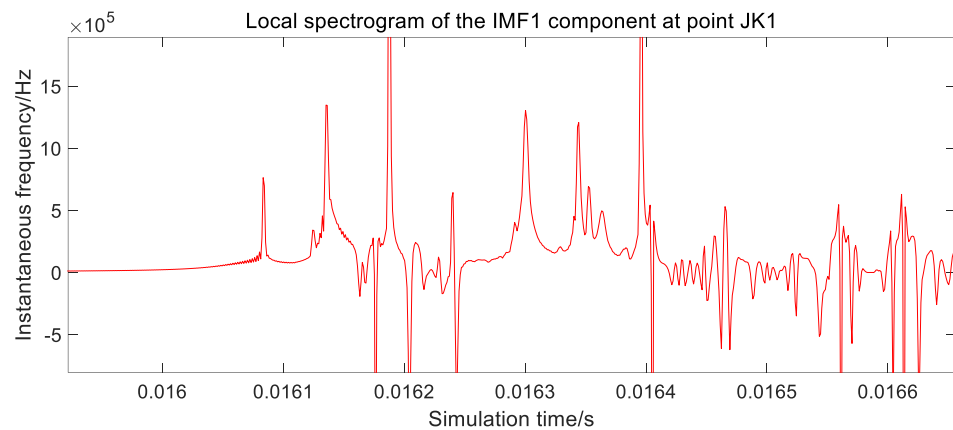

Figure 11. Local spectrogram of the IMF1 component at point JK_1.

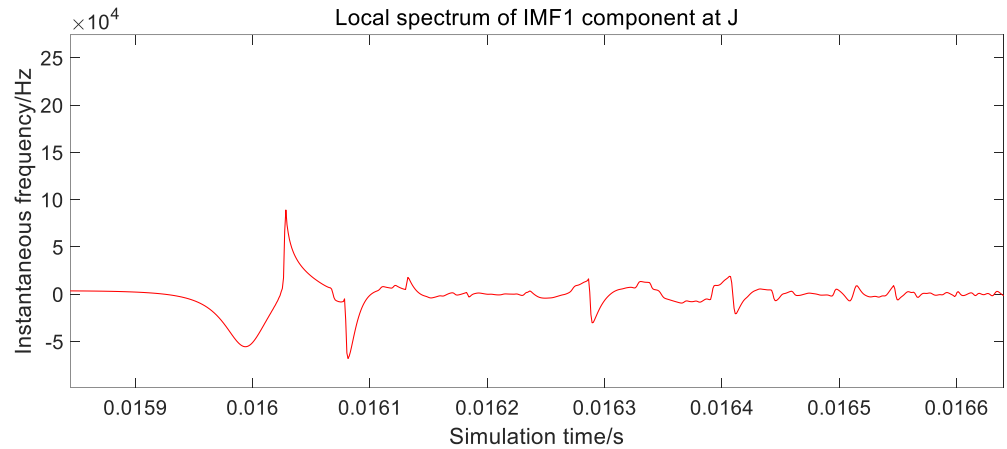Where the local spectra of the IMF1 components at point J is as follow (Figure 12).

Figure 12. Local spectrum of IMF1 component at J.

Where the local spectra of the IMF1 components at point K is as follow (Figure 13).
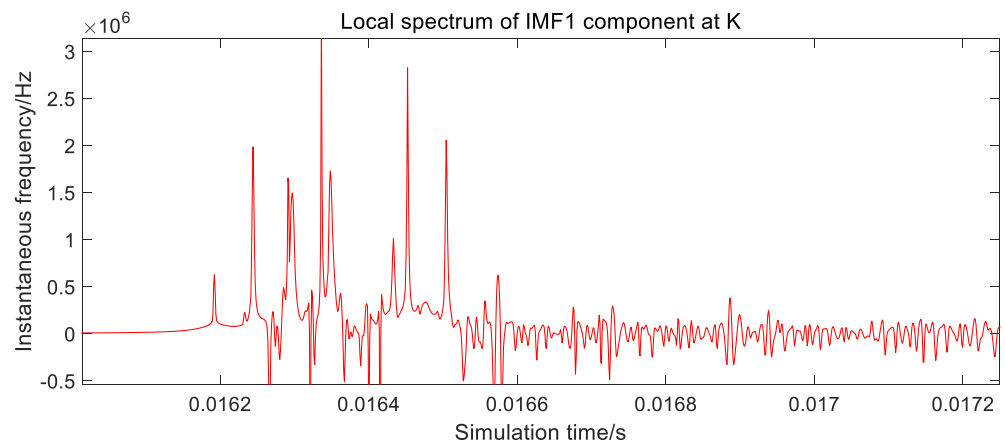

Figure 13. Local spectrum of IMF1 component at K. (Overhead line fault location).

Analysis of the instantaneous spectrum shows that the first arrival time of the fault travelling wave at point J is 0.0160283 s, so the first arrival time of the fault travelling wave at point JK1 is 0.0160833 s, and the first arrival time at point K is 0.0161923. The location of the fault at 6.19 km can be obtained by calculating Equation 9 of the principle of the three-terminal line wave method introduced above.

(2) Cable fault location

Considering the occurrence of a single-phase ground fault at 54 km of the cable section, EMD decomposition of the zero-mode components of K, KL_1, and L is carried out, and the Hilbert transform of each IMF1 component obtained is used to obtain their local transient spectra, which are shown in Figures 14–16.

Analysis of the instantaneous spectrum shows that the first arrival time of the fault travelling wave at point K is 0.0160463 s, so the first arrival time of the fault travelling wave at point KL_1 is 0.0160683 s, and the first arrival time at point L is 0.0161803. The location of the fault at 54.018 km can be obtained by calculating Equation (9) of the principle of the three-terminal line wave method introduced above.
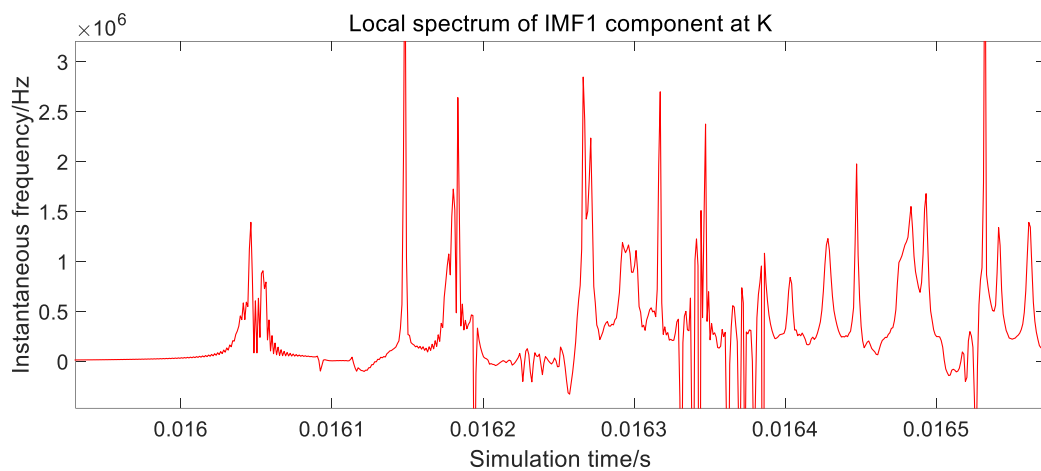
Figure 14. Local spectrum of IMF1 component at K. (Cable fault location).
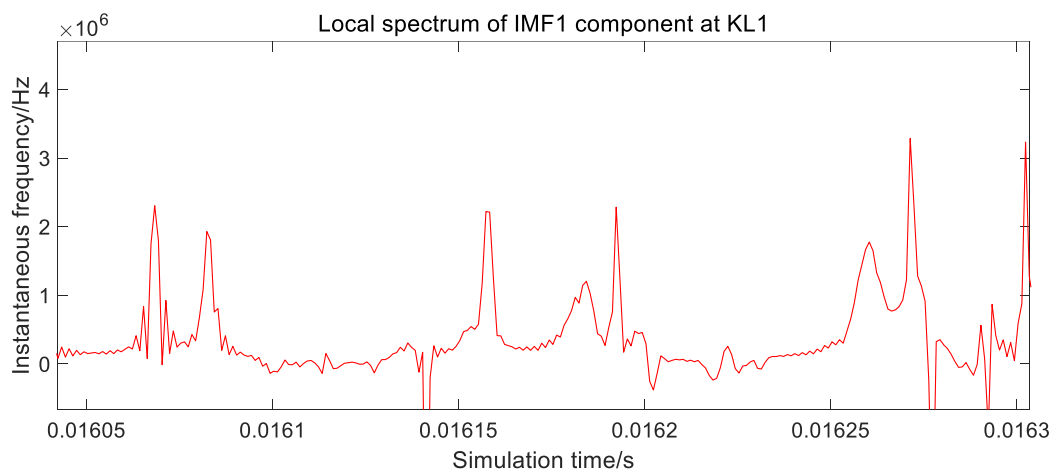

Figure 15. Local spectrum of IMF1 component at KL_1.
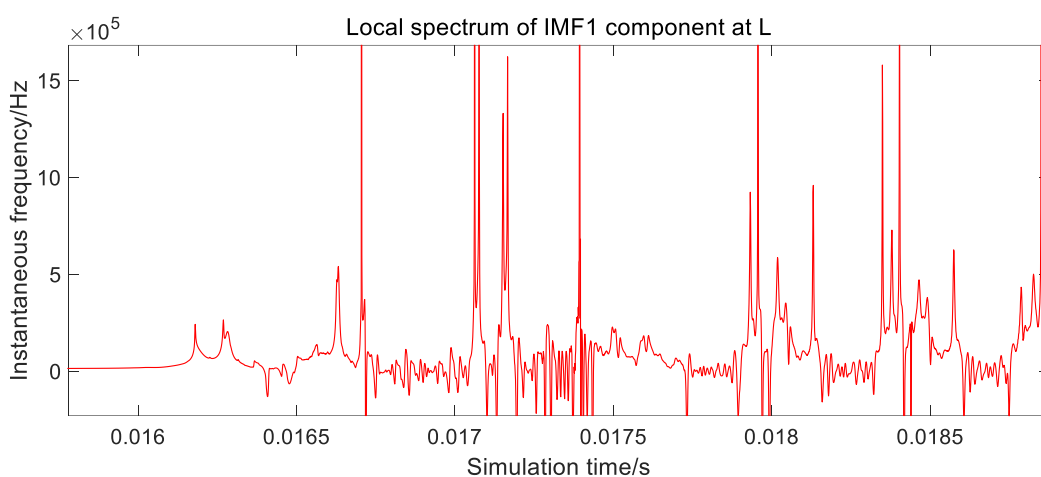

Figure 16. Local spectrum of IMF1 component at L.

Regarding the 11 km, 34 km, and 63 km fault locations, as in the above analysis, the simulation results of the three-terminal travelling wave method obtained the different fault ranges and distance measurement error values, which are shown in Table 5.

Table 5. Simulation results of the three-terminal travelling wave method at different fault locations.

| Fault Location	Fault Ranging	Distance Measurement Error $\varepsilon\%$
6 km	6.019 km	0.38%
34 km	34.060 km	0.12%
54 km	54.018 km	0.09%
63 km	64.330 km	1.65%
Branch I 6 km	6 km	0%
Branch I 33 km	32.991 km	0.09%

5.4. Comparative Analysis of Three Travelling Wave Ranging Methods

The results derived from using the single-ended, double-ended, and triple-ended travelling wave methods to obtain the fault location errors for different fault locations are shown in Table 6.

Table 6. Simulation results of three travelling wave ranging methods for different fault locations.

Failure Location /km	Failure Distance Measurement/km			Distance Measurement Error $\varepsilon\%$		
	Single Ended Method	Double Ended Method	Three Terminal Method	Single Ended Method	Double Ended Method	Three Terminal Method
6	5.587	5.925	6.019	6.88	1.25	0.38
34	34.462	36.581	34.06	13.59	7.59	0.12
54	52.811	54.87	54.018	22.02	1.88	0.09
63	63.453	60.01	64.33	7.19	4.98	1.65
Branch I 6 km	7.626	5.467	6	5.42	1.78	0
Branch I 33 km	34.226	31.12	32.991	12.26	1.88	0.09

To better elucidate that the three-terminal travelling wave method has higher accuracy, the Table 6 was plotted as a bar graph, as shown in Figure 17.
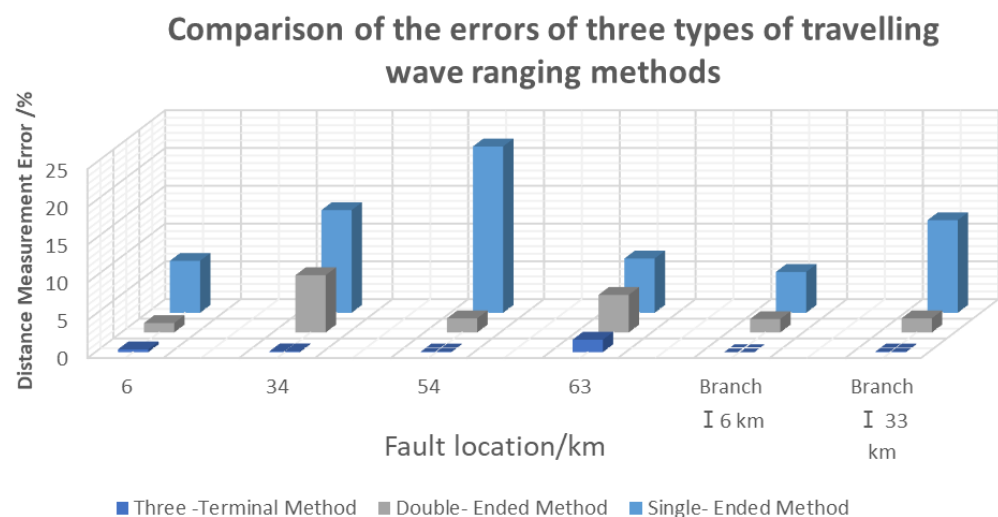
Figure 17. Comparison of the errors of three types of travelling wave ranging methods.

As can be seen from Figure 17, the three-terminal travelling wave method has a smaller measurement error and good range stability compared to the single- and double-ended travelling wave methods.

5.5. Comparison of Simulation Results Based on the Three-Terminal Travelling Wave Method under Different Analysis Methods

Due to the different sampling frequencies, the detected fault travelling wave consists of discrete points with different time intervals, and when the fault travelling wavehead is located between two sampling points, the exact location of the fault travelling wavehead cannot be obtained accurately. In this section, the sampling error correction method proposed in Section 4 is simulated and analysed on the basis of the three-terminal travelling wave method. After HHT of the zero-mode component of the faulty travelling wave (carried out according to the previous section), the approximate arrival time of the wavehead was determined, and the local zero-mode component was derived and substituted into the sampling error correction Formulas (3)–(20) to calculate the fault distance.

In order to verify that the HHT algorithm after sampling error correction has high accuracy, it was analysed and compared with the wavelet transform method fault location results; the resulting zero-mode components were subjected to wavelet transform with the basis function of db5 scale parameter of 3, and the mode value of the singularity was large enough to be extracted after selecting a suitable threshold, and the wavehead was determined to reach the measurement point moment, and the fault distance was calculated by substitution into the three-terminal travelling wave method.

The simulation results of fault location using three different methods based on the three-terminal travelling wave method using wavelet transform, HHT, and HHT combined with the sampled error correction at different fault locations are shown in Table 7.

Table 7. Simulation results of the three-terminal travelling wave method at different fault locations under different analysis methods.

Fault Location/km	Fault Ranging/km			Distance Measurement Error ε/%		
Distance Measurement Algorithm	Wavelet Transform	HHT	HHT + Sampling Error Correction	Wavelet Transform	HHT	HHT + Sampling Error Correction
6	6.818	6.019	6.003	1.636	0.38	0.06
34	34.375	34.06	34.045	0.75	0.12	0.09
54	54.167	54.014	54.016	0.835	0.09	0.08
63	62.5	64.33	62.988	2.5	1.65	0.05
Branch I 6 km	6.276	6	6	0.92	0	0
Branch I 33 km	33.12	32.991	32.005	1.2	0.09	0.05

The 3D bar charts of the error results of the three-band travelling wave method with different signal extraction methods at different fault locations are shown in Figure 18 below.
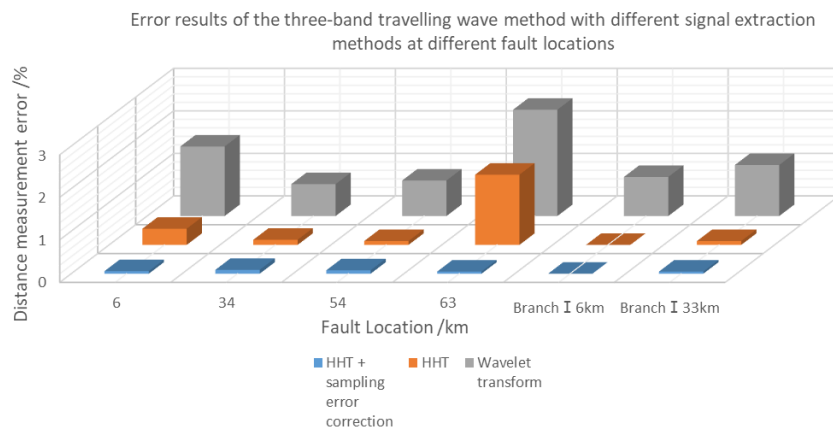

Figure 18. Error results of the three-band travelling wave method with different signal extraction methods at different fault locations.

From the above analysis, it can be seen that the range error of the three-terminal travelling wave method using wavelet transform and HHT for different fault locations is greater than the range error derived from using the combined method of HHT and sampling error correction proposed above, and the range error under this method was less than 1%, which meets engineering requirements.

5.6. Simulation Analysis of Hybrid Overhead Lines Based on the Three-Terminal Travelling Wave Method for Short Circuits Due to Different Transition Resistances

When faults occur at different locations, the contact objects between the fault point and the earth are also varied, resulting in different transition resistances, and to verify that the three-terminal travelling wave method of combined with HHT and sampling error correction has strong adaptability under different transition resistance conditions, the simulation analysis in this subsection was carried out according to the above method.

This subsection was a similar location to the one in which a fault occurred in the 6 km overhead line section in the example used for the different transition resistance short circuit simulation analysis; the metallic short circuit and transition resistance had values of 50 Ω, 75 Ω, and 100 Ω, respectively. The bus J side, overhead line cable junction point K and bus L side by different transition resistance short circuit waveform is as follows (Figure 19).
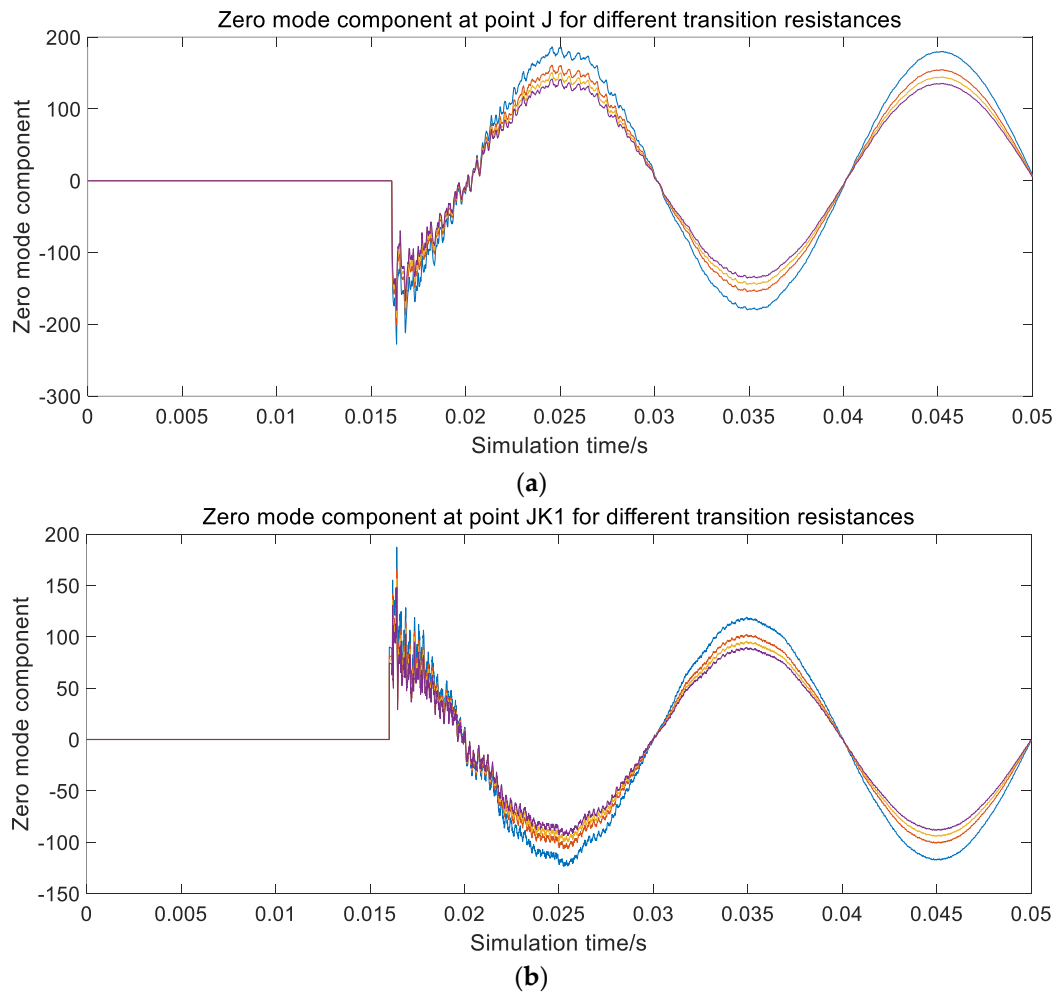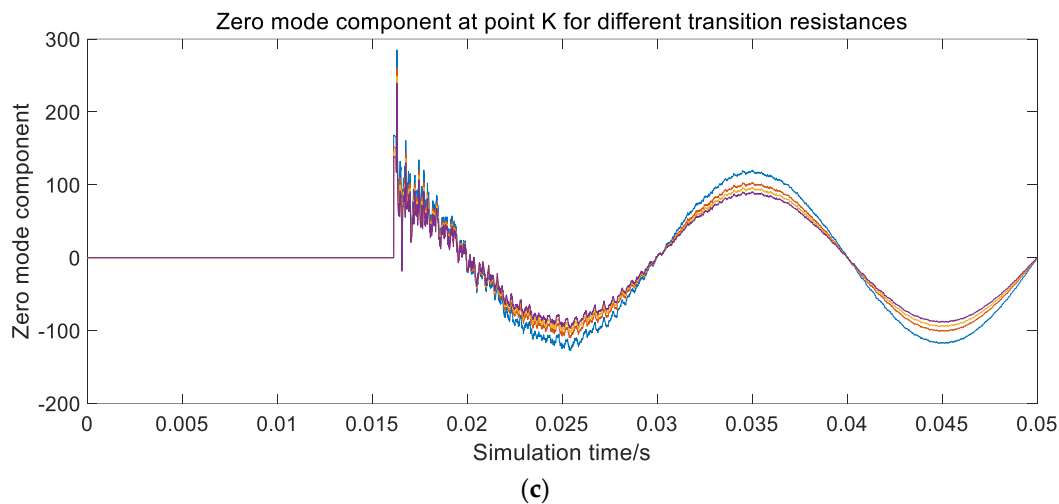

(a)

(b)

Figure 19. *Cont.*

(c)

Figure 19. Waveforms of zero-mode components at points J, JK_1, and K for different transition resistance short circuits. (**a**) Zero-mode component at point J for different transition resistances. (**b**) Zero-mode component at point JK_1 for different transition resistances. (**c**) Zero-mode component at point K for different transition resistances.

From the above figure, it can be seen that the different transition resistance values only affect the magnitude of the zero-mode current component and not the trend and location of the sudden change in the zero-mode current component waveform. Therefore, in the case of a short circuit across different transition resistances, determining both the fault segment by using the waveform similarity and the fault location by using the sudden change in the wavehead of the fault travelling wave are still applicable.

Based on different fault locations via metallic short circuit and the transition resistances of 50 Ω, 100 Ω, 200 Ω, the fault zone Pearson correlation coefficients can be determined, and the results are shown in Table 8.

Table 8. Pearson correlation coefficients at points J, K, and L for different transition resistances.

Fault Location /km	Transition Resistance /Ω	$\rho(J,K)$	$\rho(J,L)$	$\rho(K,L)$	Fault Section
6	Gold property short circuit	−0.9589	−0.9269	0.9157	
	50	−0.9365	−0.9221	0.9048	Overhead line
	75	−0.9425	−0.9236	0.9024	JK segment
	100	−0.9365	−0.9208	0.9007	
34	Gold property short circuit	−0.9796	−0.9501	0.9258	
	50	−0.9776	−0.9482	0.9207	Overhead line
	75	−0.9756	−0.9456	0.9160	JK segment
	100	−0.9719	−0.9437	0.9074	
54	Gold property short circuit	0.9936	−0.9166	−0.9083	
	50	0.9934	−0.9167	−0.9079	Cable
	75	0.9932	−0.9168	−0.9176	KL segment
	100	0.9929	−0.9169	−0.9072	
63	Gold property short circuit	0.9932	−0.9365	−0.9301	
	50	0.9727	−0.9366	−0.9266	Cable
	75	0.9668	−0.9383	−0.9212	KL segment
	100	0.9718	−0.9336	−0.9086	

Pearson's correlation coefficients at points D, E, and F for different transition resistances are in Table 9 below.

Table 9. Pearson's correlation coefficients at points D, E, and F for different transition resistances.

Fault Location /km	Transition Resistors /Ω	$\rho(D,E)$	$\rho(D,F)$	$\rho(E,F)$	Fault Section
Branch I 6 km	Gold property short circuit	0.1784	−0.2713	0.0297	Overhead line DE segment
	50	0.1757	−0.2724	0.0278	
	75	0.1745	−0.2730	0.0269	
	100	0.1733	−0.2783	0.0261	
Branch I 33 km	Gold property short circuit	0.9998	−0.2057	−0.2062	Overhead line EF segment
	50	0.9998	−0.2033	−0.2039	
	75	0.9997	−0.2024	−0.2030	
	100	0.9997	−0.2017	−0.2022	

Based on different fault locations via metallic short circuit and transition resistances of 50 Ω, 100 Ω, 200 Ω, the three-terminal travelling wave ranging method sampling error correction was used to obtain the fault location ranging results shown in Table 10.

Table 10. Simulation results of the three-terminal travelling wave method for fault location via different transition resistances short circuits.

Fault Location /km	Transition Resistors /Ω	Fault Ranging /km	Distance Measurement Error ε /%
6	Gold property short circuit	6.008	0.016
	50	5.979	0.042
	75	6.042	0.085
	100	6.003	0.060
34	Gold property short circuit	33.995	0.010
	50	33.995	0.010
	75	34.025	0.049
	100	34.045	0.090
54	Gold property short circuit	54.010	0.050
	50	53.986	0.068
	75	54.015	0.074
	100	54.016	0.008
63	Gold property short circuit	62.993	0.035
	50	62.991	0.045
	75	62.991	0.045
	100	62.988	0.063
Branch I 6 km	Gold property short circuit	5.423	0.019
	50	6.027	0.090
	75	6.029	0.096
	100	6	0
Branch I 33 km	Gold property short circuit	34.007	0.033
	50	34.017	0.083
	75	34.006	0.032
	100	32.991	0.090

As can be seen from the data in Table 10, the proposed algorithm can accurately determine the fault zone when short-circuited by different transition resistances, and the determination results are all consistent with the fault zone, and the fault distance error using the three-terminal travelling wave method is mostly less than 1%, which meets the distance accuracy requirements.

5.7. Simulation Results Based on the Three-Terminal Travelling Wave Method for Different Short-Circuit Faults

Two-phase grounded short circuits can cause damage to electrical equipment, system overvoltage, insulation breakdown, and other hazards. Three-phase short-circuits can cause high short-circuit currents, excessive forces on electrical equipment, temporary drops in system voltage, and other hazards. The hazards caused by the two short circuits are enormous. This subsection simulates the BC two-phase ground fault and the three-phase fault and calculates the fault distance and the distance error at different fault locations for the two faults, and the simulation results are shown in Tables 11 and 12.

Table 11. Simulation results of the three-terminal travelling wave method at different fault locations for BC ground shorts.

Fault Location	Fault Ranging	Distance Measurement Error ε%
6 km	6.042 km	0.08%
34 km	34.029 km	0.06%
54 km	54.015 km	0.07%
63 km	63.015 km	0.08%
Branch I 6 km	6.02 km	0.07%
Branch I 33 km	33.008 km	0.09%

Table 12. Simulation results of the three-terminal travelling wave method at different fault locations during a three-phase short circuit.

Fault Location	Fault Ranging	Distance Measurement Error ε%
6 km	6.008 km	0.02%
34 km	34.019 km	0.04%
54 km	54.005 km	0.03%
63 km	63.008 km	0.04%
Branch I 6 km	6.012 km	0.04%
Branch I 33 km	33.005 km	0.05%

As can be seen from the data in Tables 11 and 12, the proposed algorithm is able to accurately determine the fault zones when different faults occur, and the results are all consistent with the zones in which the faults occur.

6. Conclusions

By collecting the fault current travelling wave at each point on the transmission line and using the improved phase mode transform, Pearson correlation coefficients, and HHT for decoupling and fault section judgement, the fault point was finally located via using the three-terminal travelling wave method and sampling error correction. Experiments were performed using MATLAB (ver. R2021a) simulation software to verify the universality of the method.

We used Pearson's correlation coefficient to measure waveform similarity, which reduces the difficulty of fault location for hybrid lines to single overhead lines or cable lines. The HHT was used to analyse the zero-mode component of the fault and correct the sampling error, and the fault section determination was combined with the three-terminal travelling wave method to improve the ranging accuracy.

The model of the dual power supply network was established in MATLAB/Simulink, and six fault points were selected for the simulation experiments. The influence of different sampling frequencies on the range accuracy was analysed, and it was proven that the range error decreases as the sampling frequency increases. By comparing the single-ended, double-ended, and triple-ended travelling wave methods, it was proven that the triple-ended travelling wave method has the advantage of higher ranging accuracy.

It was verified that the locating results of HHT combined with the sampling error method are better than the locating results of single wavelet transform and HHT. Simulation experiments were carried out by selecting different transition resistances and various short-circuit faults, and the results show that the method can accurately determine and locate faults under various fault conditions, and the locating error is less than 1%, which meets the engineering requirements.

Author Contributions: W.C. proposed the initial idea and gave complete guidance and checked the logic of the whole article. L.Z. carried out the specification of the plan and wrote the article. Z.L. and J.C. were involved in the construction of the transmission system model, and M.X. and R.N. were involved in the preparation of the parameters. All authors have read and agreed to the published version of the manuscript.

Data Availability Statement: The data that support the findings of this study are available from the corresponding author upon reasonable request.

Conflicts of Interest: The authors declare that the research was conducted in the absence of any commercial or financial relationships that could be construed as a potential conflict of interest.

References

1. Ramar, K.; Low, H.S.; Ngu, E.E. One-end impedance based fault location in double-circuit transmission lines with different configurations. *Int. J. Electr. Power Energy Syst.* **2015**, *64*, 1159–1165. [CrossRef]
2. Deng, H.; Geng, L. Analysis of the impedance measurement of transmission lines with two-phase short circuit. In Proceedings of the 2011 International Conference on Consumer Electronics, Communications and Networks (CECNet), IEEE, Xianning, China, 16–18 April 2011; pp. 1063–1066.
3. Zhang, X.; Xu, Y.; Wang, Y.; Sun, Q.; Wang, Z.; Sun, Y. A double-end fault ranging algorithm based on parameter detection. *Power Syst. Prot. Control* **2011**, *39*, 106–111.
4. Yang, J. Application of traveling wave ranging technology on transmission lines. *Technol. Innov.* **2019**, *22*, 152–153+155.
5. Teng, L.; Liu, W.; Li, Y.; Li, G.; Qin, H. A practical new accurate algorithm for double-end ranging of high-voltage transmission line faults. *Power Syst. Autom.* **2001**, *18*, 24–27.
6. Styvaktakis, E.; Bollen, M.H.J.; Gu, I.Y.H. A fault location technique using high frequency fault clearing transients. *IEEE Power Eng. Rev.* **1999**, *19*, 58–60. [CrossRef]
7. Wu, L.; He, Z.; Qian, Q. Frequency domain method for single-ended traveling wave fault ranging. *Chin. J. Electr. Eng.* **2008**, *25*, 99–104.
8. Zhang, Y.Y.; Zhu, Y.L.; Zhang, N. Fault location of T-type transmission lines based on traveling wave inherent frequency and VMD. *Electr. Meas. Instrum.* **2017**, *54*, 55–60.
9. Xu, G.; Gong, Q.; Li, X.; Zhang, Y. Single-end fault ranging method based on atomic decomposition and traveling wave natural frequency. *Power Autom. Equip.* **2014**, *34*, 133–138.
10. Xu, J.M.; Wei, W.W.; Xia, P. Intrinsic frequency method for transmission line fault location based on Prony's algorithm. *Electr. Meas. Instrum.* **2011**, *48*, 19–24.
11. Li, C. Research on Double-End Traveling Wave Ranging Method for AC Transmission Lines. Master's Thesis, Shandong University, Jinan, China, 2017.
12. Zhang, F.; Liang, J.; Zhang, L.; Mou, Z. A new method for transmission line fault ranging based on three-terminal traveling wave measurement data. *Power Syst. Autom.* **2008**, *8*, 69–72.
13. Qi, X.; Gao, Y.; Li, Y. A T-shaped line traveling wave fault ranging method. *J. Shandong Univ. Sci. Technol. (Nat. Sci. Ed.)* **2012**, *26*, 74–77.
14. Duan, K.; Fan, Y.; Wang, Y.; Luo, R. Ranging method for ultra-high voltage DC lines considering wave speed and arc sag effect. *J. Power Syst. Autom.* **2020**, *32*, 21–27.
15. Wang, S.; Chen, X.; Xiang, Z.; Ye, Y. Distribution network single-phase ground fault selection and discrimination based on current distortion. *Autom. Technol. Appl.* **2022**, *41*, 15–18. [CrossRef]

16. Gan, Y.; Xing, Z. Fault location study based on a novel phase-to-mode transformation matrix. *Electr. Switch.* **2015**, *53*, 54–56.
17. Li, X.; Liu, Q.; Li, L. Combined fault ranging method for waveheads of hybrid lines in distribution networks based on single-end traveling wave method. *J. N. China Electr. Power Univ. (Nat. Sci. Ed.)* **2014**, *41*, 55–60.
18. Ji, T.; Sun, T.J.; Xu, B.Y.; Chen, P.; Xue, Y.R. Double-end traveling wave fault ranging technology for distribution hybrid lines. *Chin. J. Electr. Eng.* **2006**, *26*, 89–94.
19. Li, Z.; Zeng, X.; Xu, X.; Yao, J.; Zhang, X. A new algorithm for double-end traveling wave fault location on transmission lines. *Power Syst. Autom.* **2006**, *30*, 40–43.
20. Liu, Y.; Sheng, G.; Wang, Q.; Song, L.; Zhang, J.; Jiang, X. Distributed integrated fault location method for transmission lines and its simulation analysis. *High Volt. Technol.* **2011**, *37*, 923–929.
21. Wang, K.; Tang, Y.; Chen, P.; Gao, Y. Fault ranging method for high-voltage overhead line-cable hybrid lines based on combined traveling wave principle. *Power Syst. Prot. Control* **2012**, *40*, 90–94.
22. Ding, J. Research on Traveling Wave Fault Location Method for Complex Transmission Lines Based on Distributed Current Detection. Ph.D. Thesis, Shanghai Jiaotong University, Shanghai, China, 2019.
23. Bu, F.; Chen, J.; Zhang, Q.; Tian, S.; Ding, J.; Zhu, B. A controlled refinement method for load pattern identification based on two-layer iterative clustering analysis. *Power Grid Technol.* **2018**, *42*, 903–913.
24. Li, L. Research on Fault Identification and Ranging Methods for High-Voltage Transmission Lines. Master's Thesis, Tianjin University of Technology, Tianjin, China, 2021.
25. Xu, J.M.; Wang, F.Z.; Yin, X.; Xia, P. Hilbert-Huang transform-based traveling wave method for fault location on high-voltage transmission lines. *Power Syst. Prot. Control* **2012**, *40*, 88–92+105.
26. Zhang, X.-L.; Zeng, X.-J.; Ma, H.-J.; Li, Z.-W. A Hilbert-Huang transform-based traveling wave localization method for grid faults. *Power Syst. Autom.* **2008**, *8*, 64–68.
27. Liao, X.; Zhao, X.; Liang, H. A power cable fault ranging method based on Hilbert-Huang transform. *Power Syst. Prot. Control* **2017**, *45*, 20–25.
28. Ai, Y.; Chen, J.; He, J.; Feng, Q.; Lin, P.; Huang, Y. Research on HHT traveling wave fault ranging based on three-terminal method. *Electr. Meas. Instrum.* **2015**, *52*, 1–16.
29. Li, Z. Hilbert-Huang transform based application in power system fault detection. In Proceedings of the 2009 International Workshop on Intelligent Systems and Applications, IEEE, Wuhan, China, 23–24 May 2009; pp. 1–4.
30. Yang, A.K. A Single-Ended Traveling Wave Fault Location Method Based on VMD and SDEO. Master's Thesis, Wuhan University, Wuhan, China, 2018.